Imaging the construction of capillary networks in the neonatal mouse brain

Vanessa Coelho-Santos[a,b], Andrée-Anne Berthiaume[a,c], Sharon Ornelas[a], Heidi Stuhlmann[d], and Andy Y. Shih[a,b,e,1]

[a]Center for Developmental Biology and Regenerative Medicine, Seattle Children's Research Institute, Seattle, WA 98101; [b]Department of Pediatrics, University of Washington, Seattle, WA 98195; [c]Department of Neuroscience, Medical University of South Carolina, Charleston, SC 29425; [d]Department of Cell and Developmental Biology, Weill Cornell Medical College, New York, NY 10065; and [e]Department of Bioengineering, University of Washington, Seattle, WA 98195

Edited by Mark T. Nelson, University of Vermont, Burlington, VT, and approved May 23, 2021 (received for review January 15, 2021)

Capillary networks are essential for distribution of blood flow through the brain, and numerous other homeostatic functions, including neurovascular signal conduction and blood–brain barrier integrity. Accordingly, the impairment of capillary architecture and function lies at the root of many brain diseases. Visualizing how brain capillary networks develop in vivo can reveal innate programs for cerebrovascular growth and repair. Here, we use longitudinal two-photon imaging through noninvasive thinned skull windows to study a burst of angiogenic activity during cerebrovascular development in mouse neonates. We find that angiogenesis leading to the formation of capillary networks originated exclusively from cortical ascending venules. Two angiogenic sprouting activities were observed: 1) early, long-range sprouts that directly connected venules to upstream arteriolar input, establishing the backbone of the capillary bed, and 2) short-range sprouts that contributed to expansion of anastomotic connectivity within the capillary bed. All nascent sprouts were prefabricated with an intact endothelial lumen and pericyte coverage, ensuring their immediate perfusion and stability upon connection to their target vessels. The bulk of this capillary expansion spanned only 2 to 3 d and contributed to an increase of blood flow during a critical period in cortical development.

capillary | brain | angiogenesis | venule | pericyte

The brain is the most energy-demanding organ in the body. The human brain relies on dense capillary networks for the continuous distribution of blood to some 80 billion neurons. Decades of work have contributed to a rich understanding of molecular and cellular mechanisms underlying capillary angiogenesis (1). However, there remains sparse knowledge on how capillary networks are constructed in vivo, particularly in the mammalian brain where their role is so vital for uninterrupted nutritional supply. Capillary beds not only are a vast distribution chain for blood but also serve other important homeostatic functions. For instance, capillaries contribute greatly to cerebral blood flow resistance (2) particularly in the upper cortical layers (3), and parameters such as lumen diameter are carefully tuned to ensure proper blood flow rate (4) and extraction of blood oxygen (5). Capillaries are also the primary locus of the blood–brain barrier (BBB), a highly selective border that regulates passage of molecules into the brain (6). Recent studies have also cast exciting new roles for brain capillaries, including their ability to serve as a sensory web to conduct neural signals upstream to arterioles during neurovascular coupling (7), and as a source of neurotrophic signals to maintain neuronal health throughout adulthood (8). Thus, the proper construction of brain capillary networks during development is essential to brain health and homeostasis in adulthood.

The primary vascular networks of arterioles and venules in the brain are largely set during embryonic stages by vasculogenesis and angiogenesis (9, 10), and refined during very early postnatal stages (11). However, most of the subsurface capillary beds that bridge these networks are established in a second phase of angiogenesis during postnatal development (12), shaped both by blood flow and the concurrent maturation of neuronal circuitry (13). Lessons from studying development of mouse heart and retina, zebrafish fin, brain and spinal cord, and skin wound repair, have shown that veins are a source of angiogenic sprouts (14–17). In this process, venous endothelial cells dedifferentiate and are then reprogrammed to take on phenotypes of capillaries, precapillary arterioles, and arterioles as they grow and connect to the existing vascular bed. This mechanism is logical, as veins experience lower flow rates and intravascular pressure, allowing fragile sprouts to grow in a stable environment prior to their connection to high-pressure arterioles (18). However, it remains unknown whether cerebral veins contribute to the creation of tortuous and highly interconnected brain capillary networks during development.

To address this open issue, we used a longitudinal in vivo two-photon imaging approach to directly visualize the expansion of capillary networks in cerebral cortex of neonate mouse pups. This approach preserves the intracranial environment and physiology (blood flow/pressure) that is crucial to normal development of vascular networks. The overarching aim of the study was to understand the principles of capillary network construction and the establishment of capillary perfusion during postnatal development. First, we asked whether venules of the cerebral cortex are a source of angiogenic sprouts, as would be expected with conserved mechanisms across organs and organisms. Second, we aimed to understand how blood supply can remain uninterrupted during the

Significance

The distribution of blood throughout the brain is facilitated by highly interconnected capillary networks. However, the steps involved in the construction of these networks has remained unclear. We used in vivo two-photon imaging through noninvasive cranial windows to study the engineering of capillary networks in the cerebral cortex of mouse neonates. We find that angiogenic activity originates at ascending venules, which undergo a burst of sprouting in the second postnatal week. This sprouting activity first establishes long paths to connect venules to blood input from neighboring arterioles, and then expands capillary interconnectivity with a multitude of short-range connections. Our study provides an experimental foundation to understand how capillary networks are shaped in the living mammalian brain during postnatal development.

Author contributions: V.C.-S. and A.Y.S. designed research; V.C.-S. performed research; H.S. contributed new reagents/analytic tools; V.C.-S., A.-A.B., S.O., and A.Y.S. analyzed data; and V.C.-S., A.-A.B., S.O., H.S., and A.Y.S. wrote the paper.

The authors declare no competing interest.

This article is a PNAS Direct Submission.

[1]To whom correspondence may be addressed. Email: andy.shih@seattlechildrens.org.

This article contains supporting information online at https://www.pnas.org/lookup/suppl/doi:10.1073/pnas.2100866118/-/DCSupplemental.

Published June 25, 2021.

massive growth and remodeling necessary to expand existing, perfused vascular systems. Finally, we asked how BBB integrity is maintained when immature angiogenic sprouts coexist with mature, stabilized blood vessels. Improper development of capillaries can lead to conditions of abnormal cerebral perfusion and BBB function. Understanding the principles of how brain capillary networks are constructed will lead to more effective detection of abnormal vascular development in disease, and foundational knowledge to improve repair or engineering of brain vascular networks.

Results

Imaging the Development of Cortical Capillary Networks. To image the developing cerebral cortex in vivo, we refined existing cranial window protocols for two-photon imaging of postnatal mouse pups (*SI Appendix*, Fig. S1) (12, 19). This procedure involved delicately shaving the skull with surgical blades until it was only ∼15 μm thick, allowing optical access without disrupting the intracranial milieu. The window was then overlaid with cyanoacrylate glue and a glass coverslip for added stability and improved light penetration (Fig. 1*A* and *SI Appendix*, Fig. S1). With these modifications, we were able to image the cortex over many postnatal days without disruption to the developmental process or the need for repeated surgeries (Fig. 1*B*). Pups receiving surgery and repeated imaging had identical weight gain compared to littermates receiving no surgery, anesthesia, or imaging (*SI Appendix*, Fig. S2*A*). The thinned-skull window also did not produce neuroinflammation in the underlying cortex, as we detected no difference in microglial density between cortical hemispheres and in comparison to nonsurgery littermates (*SI Appendix*, Fig. S2 *B–E*). Furthermore, no difference in microvascular length was detected compared to nonsurgery littermates at postnatal day 12 (P12) or at the weaning age of P21 (*SI Appendix*, Fig. S2 *F* and *G*).

Prior studies identified a phase of marked brain capillary bed expansion in the neonatal period (12), which we captured in more detail with a daily imaging schedule from P8 to P12 (Fig. 1*B*). This time frame roughly corresponds to 36–40 wk of gestation in humans, based on common developmental benchmarks (20). To visualize the cortical microvasculature with two-photon microscopy, dextran-conjugated fluorescent dyes were injected intravenously. Since there may be continued refinement of BBB integrity during early postnatal stages, we evaluated vascular retention of intravenous dyes (i.v. dyes) of differing molecular weight. At P4, we found that the brain vasculature was still quite permeant to 10- or 70-kDa i.v. dyes (*SI Appendix*, Fig. S3). However, by P8 extravasation of these dyes significantly reduced, and leakage was eventually undetectable by P12. This indicates that BBB integrity increases over our imaging schedule to study capillary expansion. To ensure high contrast for imaging of vascular structure, we used 2-MDa FITC-dextran for the remainder of the studies since it did not extravasate at any postnatal time point examined. In addition, we also alternated i.v. dye colors of 2-MDa dye between imaging days, to reduce ectopic dye uptake by mast cells in the pia, which would otherwise obscure imaging of pial vasculature and increase noise when imaging at depth (*SI Appendix*, Fig. S4).

Consistent with capillary expansion, the density of vessels in the capillary network increased substantially between P8 to P12 (Fig. 1*C* and Movies S1 and S2). To better understand the temporal sequence of this growth, we quantified the density of capillary junctions, a measure of network connectivity, for each day of imaging. We noted that some capillary junctions had branches that were unconnected and nonflowing, consistent with nascent angiogenic sprouts. To emphasize the occurrence of these events, we categorized the data into two groups: 1) junctions with all capillaries fully connected and flowing, or 2) total junctions regardless of whether capillaries were fully connected or not (Fig. 1*D*). Plotting these two groups together as a function of postnatal day revealed a significant difference between the curves at P9, suggesting a brief and potent period of capillary network remodeling within the 5-d period examined (Fig. 1*E* and *SI Appendix*, Fig. S5 *A* and *B*).

Visualizing the Temporal Dynamics of Sprouting Angiogenesis. Angiogenesis involves several synchronized signaling pathways. One key pathway involves angiopoietin-1 signaling through the Tie2 receptor, an endothelium-specific receptor tyrosine kinase that promotes both formation and stabilization of capillaries (21). We imaged Tie2-GFP mice where endothelial-specific GFP expression level is linked to Tie2 promoter activity (Fig. 2 *A–C*) (22). Tie2 levels have been shown to elevate during brain angiogenesis (23, 24) providing an in vivo reporter for heightened signaling during vascular remodeling. Consistent with increased vascular remodeling, GFP expression was highest at P9 and gradually diminished until P12 (Fig. 2*C* and *SI Appendix*, Fig. S6).

We directly examined the spatiotemporal organization of angiogenic sprouts in Tie2-GFP mice. Endothelial GFP fluorescence aided this process because unconnected sprouts were occasionally unfilled by the i.v. dye due to lack of patency and therefore invisible to imaging by this method. As such, merging GFP and i.v. dye fluorescent signals into a single image enhanced identification of angiogenic sprouts (Fig. 2 *D* and *E*). Given the longitudinal design of the study, we could track each sprout and determine when it had formed a connection with another region of the vascular network and become patent to i.v. dye. We quantified these characteristics and plotted them as a function of time. This revealed that sprout density peaked at P9 and gradually diminished until P12, at which time very few unconnected sprouts were detected (Fig. 2*F*, green; *SI Appendix*, Fig. S5*C*). As expected, this wave of angiogenic sprouting was followed closely by a second wave of new capillary connections as these sprouts made contact with other vessels in the existing capillary network (Fig. 2*F*, orange; *SI Appendix*, Fig. S5*D*). New connections peaked at P10, suggesting that the entire process from sprout formation to connection could take as little as 24 h. When considering the total number of new connections made, we observed that P9 to P10 were the major timepoints for establishing connectivity, and that this phase had begun to plateau by P12 (Fig. 2*G* and *SI Appendix*, Fig. S5*E*). Furthermore, the density of sprouts within a field of view correlated with Tie2 promoter activity closely (assayed by GFP fluorescence in the same field of view), further reinforcing Tie2 activity as an essential signal in sprout formation (Fig. 2*H*). Together, these data reveal ∼P9–P10 as a critical window in capillary bed construction and highlight the remarkable speed at which decisions for capillary connectivity are made.

Cortical Ascending Venules Are the Source of Angiogenic Sprouts. We next asked whether venules were a source of angiogenic activity in the brain. In order to identify and distinguish arteries from veins, we relied on both vessel anatomy at the pia and the direction of blood flow, as assessed by line-scans, i.e., arteriole blood flows into cortex, while venules flow outward (Fig. 3 *A* and *B*). These physiological characteristics have been used to unequivocally distinguish arterioles from venules in prior in vivo imaging studies (25, 26). Having established vessel type at the pial surface, the vertically oriented penetrating arterioles and ascending venules connected to these pial networks could be examined in relation to the capillary network below the brain surface (Fig. 3*C*). We quantified the number of angiogenic sprouts originating from either penetrating arterioles or ascending venules over time (Fig. 3 *D* and *E*). This revealed that ascending venules were the exclusive source of angiogenic sprouts during capillary bed formation (Fig. 3 *D* and *E*). At P9–P10, when angiogenesis was most active, these sprouts were seen to emerge directly from the ascending venule itself or its initial branching offshoots.

To further confirm the identity of penetrating arterioles and ascending venules, we imaged PDGFRβ-tdTomato; Tie2-GFP

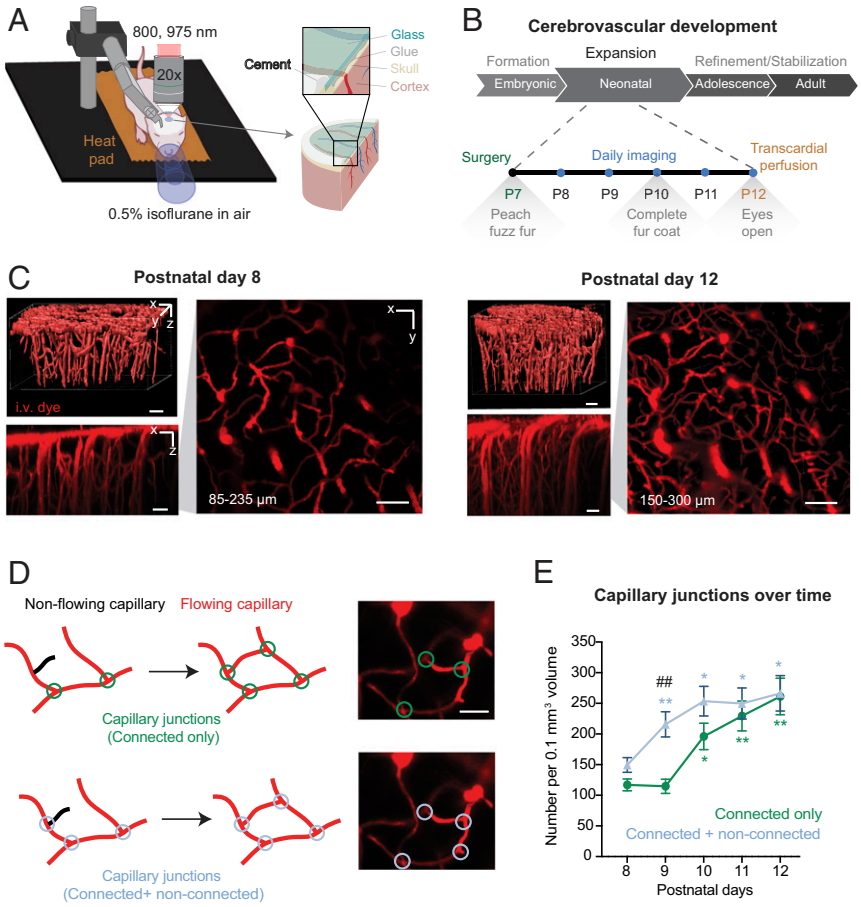

Fig. 1. In vivo imaging of postnatal vascular development in cerebral cortex. (*A*) Schematic of head-fixation apparatus used for two-photon imaging of mouse neonates, with depiction of components for chronic thinned skull window. (*B*) Timeline of cerebrovascular development. Imaging was performed during a phase of postnatal capillary expansion. Cranial windows were implanted at P7, and in vivo imaging was performed daily from P8 to P12. (*C*) Three-dimensional reconstructions of cortical microvasculature at P8 and P12. Two-dimensional images are maximal projections from the side of the image volume (*x*–*z*) and from the top of the volume (*x*–*y*). (*D*) Schematic and representative in vivo images depicting two approaches to quantify capillary branch density at each postnatal day examined: (*Top*) counting of capillary junctions including only those with all branches connected and perfused, and (*Bottom*) counting of capillary junctions irrespective of whether all capillaries were connected and perfused. (*E*) Number of capillary junctions based on two measurement approaches above plotted over time. For connected only: $*P = 0.0328$ (P8 vs. P10), $**P = 0.0073$ (P8 vs. P11), $**P = 0.005$ (P8 vs. P12); for connected plus nonconnected: $**P = 0.0031$ (P8 vs. P9), $*P = 0.0176$ (P8 vs. P10), $*P = 0.0169$ (P8 vs. P11), $*P = 0.0110$ (P8 vs. P12); indicating significant difference from P8 with each measurement approach (two-way ANOVA; Dunnett's post hoc test; postnatal days: $F_{(1.447,\ 17.37)} = 28{,}30$, $***P < 0.0001$ overall). $^{\#\#}P = 0.0092$, indicating significant difference between measurement approaches at P9 (two-way ANOVA; Sidak's post hoc test; postnatal days vs. capillary junction type: $F_{(4,\ 48)} = 3.395$, $*P < 0.0159$ overall). Data are presented as mean ± SEM ($n = 7$ mice; one region imaged per mouse).

mice, which have labeled mural cells (red) and endothelial cells (green). Smooth muscle cells are very brightly labeled and densely packed on penetrating arterioles, making it straightforward to distinguish between arterioles and venules (*SI Appendix*, Fig. S7*A*). Consistent with data from Tie2-GFP mice (Fig. 3 *A*–*E*), we observed angiogenic sprouts arising exclusively from ascending venules but not penetrating arterioles in PDGFRβ-tdTomato; Tie2-GFP mice (*SI Appendix*, Fig. S7*B*). In stark contrast to the sprouting activity of parenchymal venules, pial venules at the cortical surface that collected blood from the ascending venules, underwent regression and refinement before and during the phase of capillary angiogenesis (*SI Appendix*, Fig. S8).

To further explore whether the observed venous-derived sprouts involved endothelial programs for angiogenesis, we also imaged epidermal growth factor-like protein 7 (EGFL7) reporter mice (Fig. 3*F*). EGFL7 is involved in vascular patterning during angiogenesis, and its expression is associated with the angiogenic front (27). Studies of retinal vascular development have shown greater venous expression of EGFL7 and no colocalization with α-smooth muscle actin-positive arteries and arterioles (28). Again consistent with ascending venules being a source of angiogenesis in cerebral cortex, we observed that many emerging sprouts at the venules were Egfl7-eGFP positive (Fig. 3*G*). We noted some Egfl7-eGFP expression around penetrating arterioles, although it was not associated with angiogenic sprouts (Fig. 3*F*). Collectively, these data provide evidence that the brain capillary bed is constructed through angiogenic activity originating from ascending venules in the cerebral cortex.

Hierarchical Organization of Venous Capillary Sprouting. To better understand the spatiotemporal sequence of angiogenic sprouting from venules, we characterized their occurrence based on vascular branch order. We denoted the main trunk of ascending venules as 0th order, and the first segment of any offshoots to be first order (*SI Appendix*, Fig. S9*A*). With continued ramification, each successive branchpoint from the ascending venule increased branch order by 1. We then grouped sprouts based on the branch order from which they emerged. Results showed that earlier emerging sprouts, primarily at P9, originated at the 0th-order venule or first-order branches (*SI Appendix*, Fig. S9 *B* and *C*).

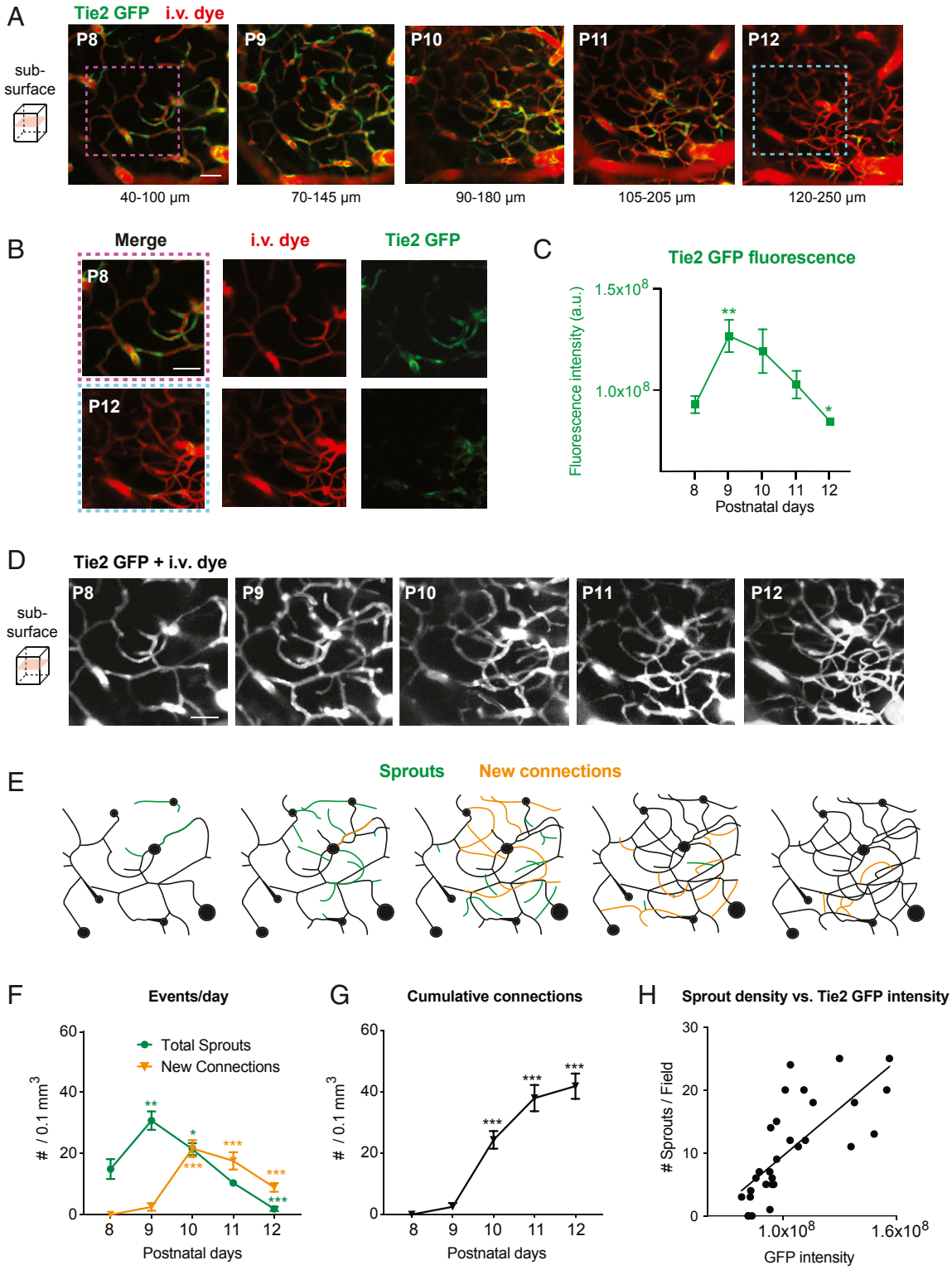

Fig. 2. Temporal dynamics of Tie2 expression and angiogenic activity. (*A*) Imaging the same capillary region from P8 to P12 reveals temporal differences in GFP fluorescence in Tie2-GFP mice. (Scale bar: 50 µm.) (*B*) *Inset* from *A* showing magnified view of GFP-positive endothelial cells and i.v. dye at P8 and P12. (Scale bar: 50 µm.) (*C*) Intensity of GFP fluorescence across the imaging field over time. $^{**}P = 0.0059$ (P8 vs. P9), $^{*}P = 0.0358$ (P8 vs. P12) [one-way ANOVA; Dunnett's post hoc test; $F_{(1.536,\ 7.682)} = 14.70$; $^{**}P = 0.0032$]. Data are presented as mean ± SEM ($n = 6$ mice; one region imaged per mouse). (*D*) Representative images of cortical microvascular architecture from P8 to P12, with i.v. dye and GFP signals overlaid to visualize both perfused vasculature and unperfused angiogenic sprouts. (Scale bar: 50 µm.) (*E*) Tracings of vasculature shown in *D* to highlight location of unconnected angiogenic sprouts (green) that are seen to connect with other regions of the capillary bed (orange) over the imaging timeline. (*F*) Number of total sprouts (green) and new connections (orange) plotted as a function of postnatal day. For total sprouts: $^{**}P < 0.0082$ (P8 vs. P9), $^{*}P < 0.0363$ (P8 vs. P10), $^{**}P < 0.0020$ (P8 vs. P12). For new connections: $^{***}P < 0.001$ (P8 vs. P10), $^{***}P < 0.0006$ (P8 vs. P11), $^{***}P < 0.0009$ (P8 vs. P12) [two-way ANOVA; Dunnett's post hoc test, postnatal days vs. events factor: $F_{(4,\ 68)} = 37.40$, $^{***}P < 0.0001$]. Data are presented as mean ± SEM ($n = 10$ mice; one region imaged per mouse). (*G*) Cumulative capillary connections over time. $^{***}P < 0.001$, compared to P8 [one-way ANOVA; Dunnett's post hoc test; $F_{(2.174,\ 18.48)} = 66.15$, $^{***}P < 0.0001$]. Data are presented as mean ± SEM ($n = 10$ mice; one region imaged per mouse). (*H*) Tie2-GFP intensity plotted as a function of the sprout density within the same field of view. Pearson's correlation: $R^2 = 0.5371$, $P < 0.0001$; $n = 30$ fields over six mice (one region imaged five separate times per mouse).

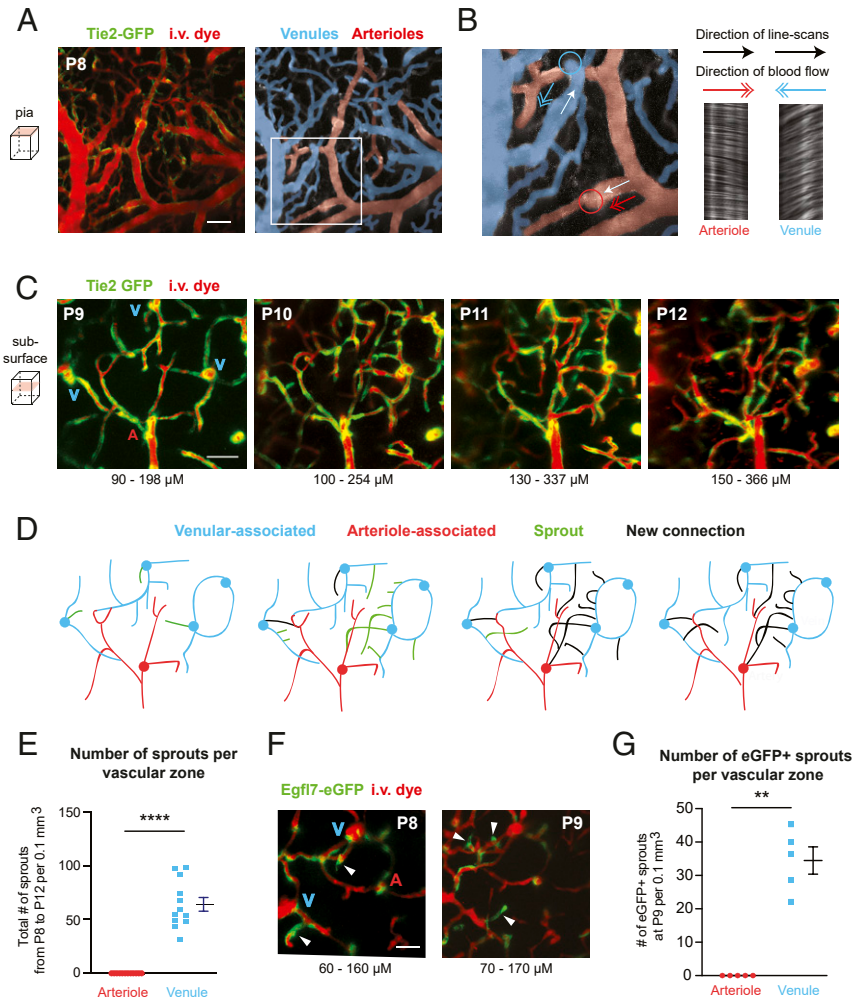

Fig. 3. Cortical ascending venules are the origin of angiogenic sprouts. (*A*) Example of pial vasculature as visualized in a Tie2-GFP mouse at P8 (*Left*). The pial arteriole network (red) and venous network (blue) are pseudocolored to aid identification. (Scale bar: 50 µm.) (*B*, *Left*) *Inset* from *A*. Line-scans were used to determine direction of blood flow to confirm arteriole or venule identity. The white arrow indicates the direction of the line-scan, and the colored arrow indicates direction of the flow. The colored circles mark the location where ascending venules emerge from or penetrating arterioles descend into the underlying cortex. (*Right*) The resulting line-scan image collected from the depicted arteriole and venule, along with direction of line-scan and direction of flow. (*C*) Maximally projected images collected below the cortical surface in a Tie2-GFP mouse with labeled endothelial cells (green) and i.v. dye (red, Alexa 680-dextran; 2 MDa). This image contains three ascending venules (V) and one penetrating arteriole (A). (Scale bar: 50 µm.) (*D*) Tracings of vasculature shown in *C* to highlight location of venule-associated (blue) and arteriole-associated (red) vessels, along with angiogenic sprouts (green) and newly made capillary connections (black). The locations where capillaries connect are not shown if their depth was out of range of the maximally projected image. (*E*) Quantification of the number of total sprouts originating from arterioles vs. venules. ***$P < 0.0001$ [paired *t* test; $t_{(11)} = 10.02$]. Data are presented as mean ± SEM ($n = 12$ mice; one region imaged per mouse). (*F*) Images of cortex from Egfl7-eGFP mice at P8 and P9. eGFP is expressed in the tip and stalk of angiogenic sprouts emerging from the ascending venules. (Scale bar: 50 µm.) (*G*) Number of eGFP-positive sprouts observed in arteriole-associated vs. venule-associated zones. **$P = 0.0011$ [paired *t* test; $t_{(4)} = 8.095$]. Data are presented as mean ± SEM ($n = 5$ mice; one region imaged per mouse).

As time progressed, sprouts emerged from higher-order branches, indicating that sprouting was occurring deeper within the capillary network (*SI Appendix*, Fig. S9 *D–F*). A plot of peak day of sprouting at each branch order clearly illustrates this graded process (*SI Appendix*, Fig. S9*G*). Thus, there is an organized and sequential pattern of sprouting with early sprouts emerging closer to the venule and later sprouts emerging deeper in the capillary network.

Characterization of Sprout Dynamics and Targeting during Angiogenesis. We next examined the characteristics of early and late-stage sprouts derived from venules and the vessels with which they connected to receive blood flow input. We found that earlier sprouts were destined to connect with penetrating arterioles or their immediate offshoots, forming direct but tortuously shaped conduits between arteriolar input and venous output (Fig. 4*A* and *SI Appendix*, Fig. S10 *A* and *B*). To achieve this task, long-range sprouts grew faster and covered larger distances to make arteriole contact (as much as 400 µm) (Fig. 4 *C* and *D*). Long-range sprouts initiated from the 0th-order ascending venule or their immediate branches between P8 and P10 (Fig. 4 *E* and *F*). In contrast, sprouts that emerged later were short-range and destined to connect with other nearby capillaries (Fig. 4*B* and *SI Appendix*, Fig. S10 *C* and *D*). Short-range, capillary-targeting sprouts grew about one third the distance of long-range sprouts (Fig. 4 *C* and *D*), and emerged primarily between P10 and P11 from higher-order branches of the ascending venule. With differences in their length, long-range sprouts required about twice the time to become patent and flowing with blood cells, compared to short-range sprouts (Fig. 4*G*). Altogether, these data show that long-range arteriole-to-venous arcs are first created to form the backbone of the capillary network, and then short-range sprouts establish greater anastomotic connectivity within the capillary bed.

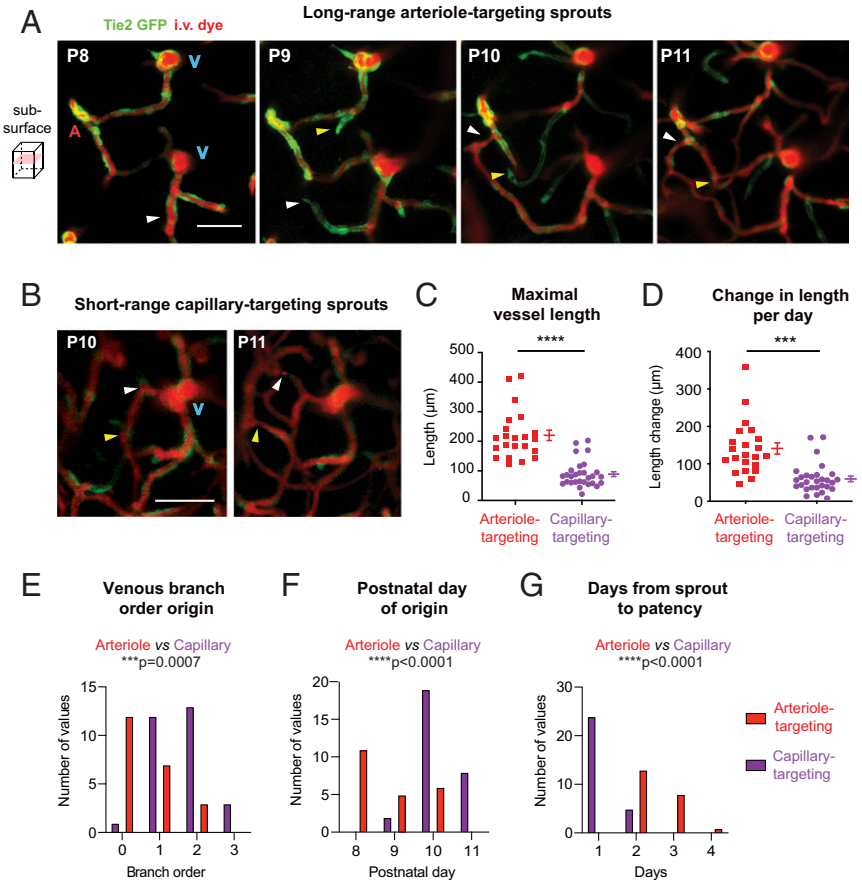

Fig. 4. Distinct spatiotemporal dynamics of venule-derived sprouts that target arterioles vs. capillaries. (*A* and *B*) Representative images of long-range arteriole-targeting sprouts (*A*) and short-range capillary-targeting sprouts (*B*). Arrowheads correspond to two examples (white or yellow) for each sprout type. (Scale bar: 50 μm.) A, artery; V, vein (also see *SI Appendix*, Fig. S10). (*C*–*G*) Different features of arteriole-targeting and capillary-targeting sprouts according to their connection target. Maximal vessel length: $^{****}P < 0.001$, $t_{(14)} = 5.980$. Change in length per day: $^{***}P = 0.0006$, $t_{(14)} = 4.409$. Venous branch order: $^{***}P = 0.0007$, $t_{(14)} = 4.298$. Postnatal day origin: $^{****}P < 0.0001$, $t_{(14)} = 6.141$. Days from sprout to patency: $^{****}P < 0.0001$, $t_{(14)} = 6.874$ (paired *t* test). Data are presented as mean ± SEM ($n = 51$ sprouts from four mice).

Pericytes and Endothelial Cell Dynamics Are Synchronized during Brain Angiogenesis. During development of new vessels, endothelial tubes are formed first and then secondarily covered by migrating pericytes, which promotes vascular stability and BBB maturation (29–31). This implies a window of endothelial immaturity prior to pericyte coverage (32), and raises questions of how BBB integrity continues to be refined (*SI Appendix*, Fig. S3), despite a significant burst of vascular remodeling. To examine this further, we studied pericyte–endothelial interplay in Tie2-GFP; PDGFRβ-tdTomato mice (*SI Appendix*, Fig. S7*B*). We found that pericytes were abundant in developing capillary networks (Fig. 5*A*). Pericyte numbers nearly doubled between P8 and P12 (Fig. 5*B*). While it was difficult to pinpoint the source of new pericytes due to a limited sampling rate, the position of pericyte somata shifted between time points, indicating their motility. Pericytes were occasionally seen to migrate from venules as new sprouts emerged, but also appeared to divide locally within the expanding capillary bed (*SI Appendix*, Fig. S11*A*). Nearly the entire endothelial network was in contact with either pericyte somata or their extensive processes (Fig. 5*C*). Even in regions that appeared sparsely covered, detailed observation revealed thin strands of tdTomato-positive pericyte processes.

We narrowed our focus to pericyte–endothelial interaction at the tips of angiogenic sprouts. We noted that sprouts could emerge from vessels that had pericyte coverage and had a tendency to emerge from locations occupied by pericyte somata (*SI Appendix*, Fig. S11 *B* and *C*). This may explain why pericyte somata are more prevalent at capillary bifurcations in the adult brain (33). Second, we found that 95% of angiogenic sprouts were contacted by thin pericyte processes. The minor fraction of sprouts uncontacted by pericyte processes were typically very short protrusions (<20 μm in length). In some cases, pericyte processes on a sprout lagged slightly behind the GFP-positive endothelial tip cell, consistent with endothelial growth followed by pericyte recruitment (Fig. 5 *C* and *D*). These sprouts were longer than those that had full pericyte contact, and in a subset of longitudinal experiments, we confirmed that these were long-range arteriole-targeting sprouts (Fig. 5*E*). In contrast, sprouts with full pericyte contact tended to make short-range connections within the capillary bed (Fig. 5*F*). Interestingly, we were able to observe increased coverage by mural cells at the precapillary zone, as seen in the adult microvasculature (34), indicating that pericyte morphology unique to the precapillary zone was established within this developmental time frame (*SI Appendix*, Fig. S11*D*).

The continual presence of pericytes implied that pericyte-mediated capillary tone could be readily established during the angiogenic process. To examine this, we quantified the diameter of long-range arteriole-targeting sprouts. An emerging sprout sometimes exhibited a small-diameter lumen visibly filled by i.v. dye (*SI Appendix*, Fig. S12*A*). Capillary diameter consistently increased when sprouts connect to their targets but remain unperfused by

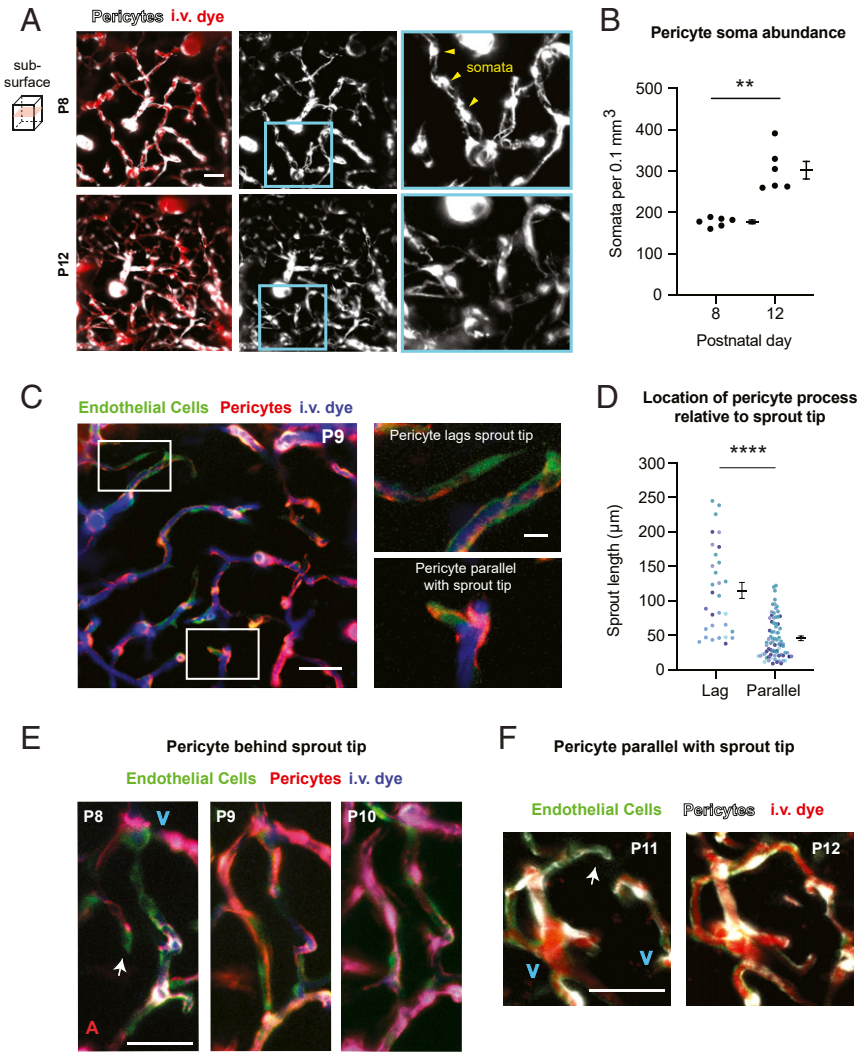

Fig. 5. Pericyte–endothelial synergy in construction of brain capillary networks. (*A*) Representative in vivo images of PDGFRβ-tdTomato;Tie2-GFP cortical vasculature, showing pericyte (white) contact with all microvasculature (red). Images of tdTomato-positive pericytes alone reveals their structure. The *Inset* marks example ovoid-shaped pericyte somata along one capillary (yellow arrowheads in *Inset*) with their intervening processes contacting the rest of the capillary. (Scale bar: 50 μm.) (*B*) Number of pericyte somata per volume at P8 and P12. $^{**}P < 0.0012$, $t_{(5)} = 6.613$ (paired *t* test). Data are presented as mean ± SEM ($n = 6$ mice; one imaged region per mouse). (*C*) High-resolution image highlighting two different arrangements of pericyte process and endothelial tip position at angiogenic sprouts: (*i*) Pericyte process lagging behind endothelial tip, or (*ii*) pericyte process parallel with endothelial tip. (Scale bar: 50 μm.) (*D*) Length of angiogenic sprouts exhibiting two arrangements of pericyte–endothelial position. $^{****}P < 0.0001$, $t_{(21)} = 6.645$ (paired *t* test). Data are presented as mean ± SEM ($n = 109$ sprouts from six mice at ages P9 and three mice at ages P10). (*E*) Example of sprout with a lagging pericyte process connecting to an arteriole. A, artery; V, vein. (Scale bar: 10 μm.) (*F*) Example of sprout with a parallel pericyte process connecting locally in the capillary bed. (Scale bar: 50 μm.)

blood cells. After blood cell perfusion began (confirmed by transit of blood cell shadows) the capillaries then consistently reduced in diameter (*SI Appendix*, Fig. S12 *B* and *C*). This suggests that sprouts are pressurized during growth and establish myogenic tone with blood cell passage.

Collectively, these data show that pericyte recruitment and coverage is tightly synchronized with endothelial sprouting. This constant pericyte coverage likely helps to maintain BBB integrity and blood flow resistance during development. Furthermore, pericyte coverage does not inhibit angiogenic activity, as sprouts were seen to emerge from established capillaries with pericyte coverage.

Effect of Capillary Expansion on Cortical Blood Flow. We next sought to understand how phasic changes in capillary remodeling affected blood supply to the cortex. To do so, we measured blood flow in penetrating arterioles and ascending venules on the pial surface, which represent the collective input and output of blood from the large regions of underlying cortical tissue, respectively. Despite ongoing refinement of the pial venules (*SI Appendix*, Fig. S8) (11, 19, 35), the location of penetrating arterioles and ascending venules were easily identifiable when imaging below the pial surface. We observed a preserved ratio of ~2–3 cortical ascending venules per every penetrating arteriole from P8 to P12 (Fig. 6 *A* and *B*). This ratio is maintained into adulthood, as studies in adult rodent cortex have made similar observations in arteriole/venous ratio (36, 37).

From P8 to P12, we first quantified the diameter of penetrating arterioles and ascending venules at the pial surface over time, just before their descent into the cortex (Fig. 6*C*). We then used two-photon line-scanning to track the speed and direction of blood cell flow in the vessel at this same location (Fig. 6 *D*–*F*) (38). Blood cell velocity and vessel width were used to calculate volume flux of blood using a modified formula based on

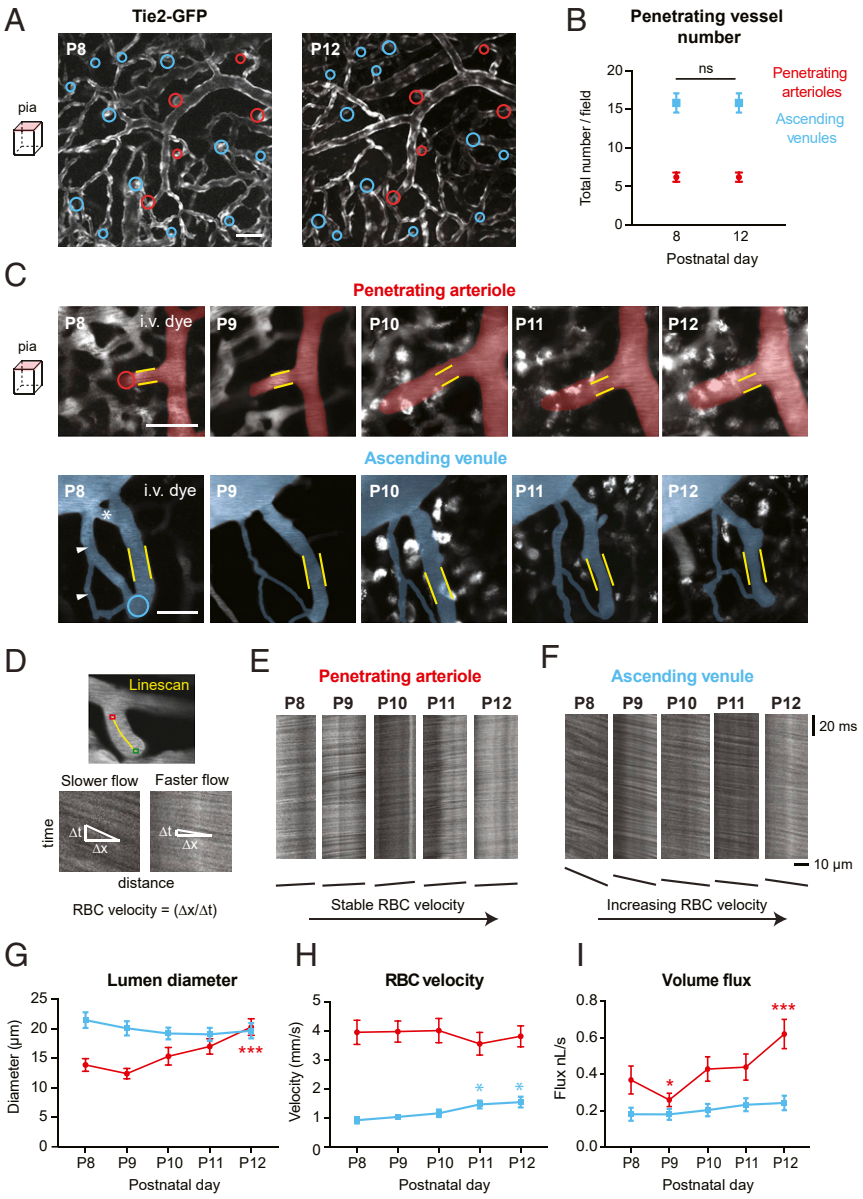

Fig. 6. Changes to penetrating arteriole and ascending venule structure and vasodynamics. (*A*) In vivo images comparing pial cortical vasculature in a Tie2-GFP mouse at P8 and P12. Penetrating arteriole and ascending venule positions are identified by red and blue circles, respectively. (Scale bar: 50 μm.) (*B*) Number of total penetrating arterioles and ascending venules does not change from P8 to P12. ns, not significant [two-way ANOVA; Sidak's post hoc test: $F_{(4,\ 144)} = 0.000$, $P > 0.99$], $n = 19$ animals; one region imaged per mouse. (*C*) Magnified view showing structural changes in a penetrating arteriole and ascending venules at the pial surface where blood velocity line-scans are taken. Yellow lines correspond to boundaries of the vessel lumen at P8, applied to subsequent postnatal time points. Red and blue circles show point of vessel descent into cortex. The white asterisk marks a venular loop that is pruned, and white arrowheads mark auxiliary venule loop that is remodeled in diameter. (Scale bar: 50 μm.) (*D*, *Top*) Example of a line-scan trajectory (yellow line), with the green and red points marking line-scan start and stop positions, respectively. Iterative scanning produces a time–space plot (*D*, *Bottom*) where the angle of the streaks formed by moving blood cells is related to the speed of flow. The horizontal dimension is distance along the line-scan path, and the vertical dimension is time. An angle that is greater from the horizontal corresponds to lower flow velocity. (*E* and *F*) Example of raw line-scan data from a penetrating arteriole (*E*) and ascending venule (*F*), collected each day of imaging. Below, lines are drawn to show the changes in streak angle over time representing velocity. (*G–I*) Change in lumen diameter (*G*), RBC velocity (*H*), and RBC volume flux (*I*) in penetrating arterioles (red) and ascending venules (blue). $n = 20$ arteries and 22 veins for *G–I*, respectively, over 10 mice for both vessel groups. Diameter over time $F_{(2,614,\ 103,9)} = 6.589$, $^{***}P = 0.0007$: $^{***}P < 0.001$ (P8 vs. P12); velocity over time, $F_{(3.449,\ 137,1)} = 0.5451$, $P = 0.6768$: $^{*}P = 0.0283$ (P8 vs. P11), $^{*}P = 0.0245$ (P8 vs. P12); flux over time, $F_{(4,\ 159)} = 13.53$, $^{***}P < 0.0001$: $^{***}P < 0.001$, compared to P8 (two-way ANOVA with Dunnett's post hoc test).

Poiseuille's law of laminar flow (39). We found that on average there was a gradual increase in the diameter of penetrating arterioles (Fig. 6*G* and *SI Appendix*, Fig. S13*A*). Curiously, a slight but nonsignificant decrease in arteriole diameter was consistently seen at P9, which corresponded to the peak of angiogenesis in the underlying capillaries. In contrast, ascending venules exhibited no major change over time (Fig. 6 *C* and *G* and *SI Appendix*, Fig. S13*B*). However, nonessential loops within the pial venule network were typically remodeled or pruned. Blood cell velocity in arterioles was generally stable over time, consistent with prior imaging studies (40), although a slight increase in venous red blood cell (RBC) velocity was seen at P12 (Fig. 6*H* and *SI Appendix*, Fig. S13). When considering volume flux, we observed an increase in blood flow from P8 to P12 in both penetrating

arterioles and ascending venules (Fig. 6*I* and *SI Appendix*, Fig. S13). Penetrating arteriole flux is higher per vessel consistent with our finding that outflow is distributed to approximately two to three ascending venules, as discussed above. Flux increase in arterioles was driven by gradual arteriole dilation and manifested in venules as an increase in flow velocity. Given that vessel diameter is the major determinant of blood flux, the slight constriction seen in arterioles at P9 caused a significant decrease in volume flux for 1 d. However, this was followed by a doubling of flux over the next 3 d.

Finally, we combined our overall findings to link the temporal characteristics of capillary network expansion to cortical blood flow dynamics. To compare the different metrics on the same scale, we normalized blood flow parameters to baseline levels for each mouse and plotted these as a group average (Fig. 7*A*). This was overlaid with metrics of capillary structure, normalized to the day of peak change. This revealed that cortical blood flow increases steadily over the time frame examined, and that this occurred in parallel with accumulation of new capillary connections. The density of new capillary connections correlated well with the magnitude of blood flow input and output in each field of view examined (Fig. 7*B*). The small but significant decrease in cortical blood input coincided with the burst of angiogenic activity at P9 (Fig. 7*A*). However, this disruption did not have a lasting effect on the trajectory of blood flow increase over time. Thus, vascular development is engineered to ensure that even during very active angiogenesis, metabolic supply to the developing cortex is minimally perturbed.

Discussion

We longitudinally imaged a phase of capillary expansion during postnatal development of the mouse cerebral cortex (Fig. 7*C*). Our results show that the multitude of distributed ascending venules that drain blood from the parenchyma of the cerebral cortex are loci for sprouting angiogenesis, sourcing all new capillary connections in a burst of neovascularization around P9–P10. We observed spatiotemporally organized early and delayed phases of angiogenic sprouting during construction of the capillary plexus. These collective neovascularization events contribute to a gradual increase in cortical blood flow and cause minimal disruption to the constancy of flow despite extensive remodeling of microvascular architecture.

The finding that venules of the brain contribute to capillary sprouting bears similarity to microvascular network construction in other vertebrate models (zebrafish) and mammalian organs (heart and retina). During heart development in the mouse, angiogenic sprouts emerge from the sinus venosus to give rise to a capillary plexus, and eventually the formation of coronary arteries (14). The formation of the capillary networks between radially alternating arteries and veins in retina also begins with sprouting around veins (17). In imaging studies of live zebrafish, small venules in the tail, hindbrain, and spinal cord were shown to give rise to angiogenic sprouts destined for connection with arterioles (15, 16, 41). These sprouts involved relatively short-range connections between closely positioned venules and arterioles, leading to the creation of ladder-like networks. In contrast, brain capillary networks are tortuous, dense, and highly interconnected. As such, the brain orchestrates a more complex program to achieve this specialized architecture. We observed an initial phase of

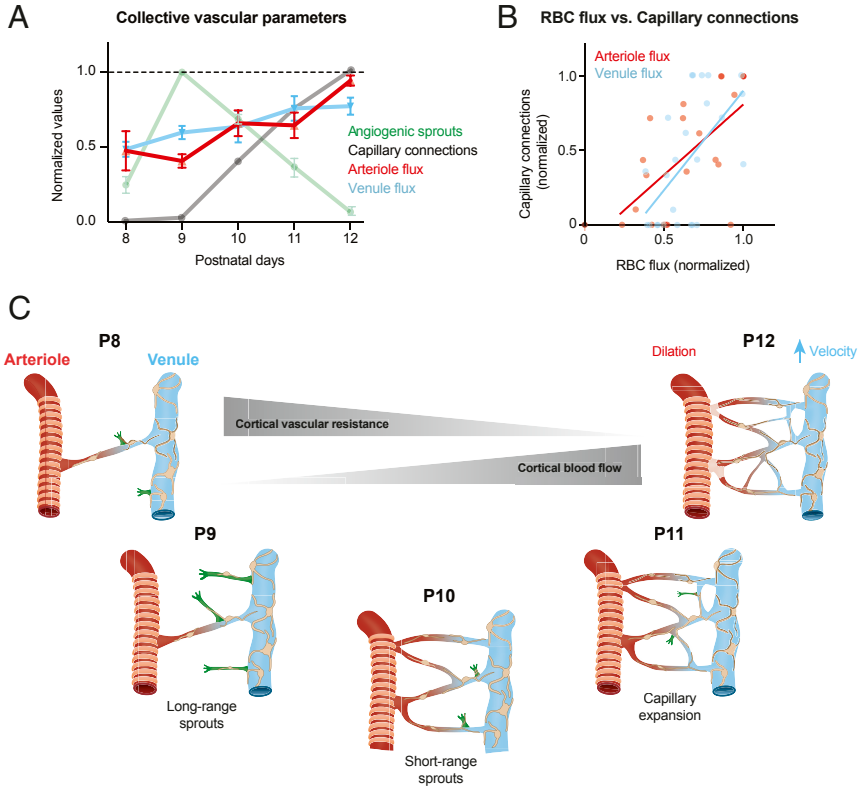

Fig. 7. Impact of capillary bed growth and expansion on blood flow. (*A*) Compendium of structural and blood flow changes over time, normalized for comparison. (*B*) Correlation between number of new capillary connections and the flux of penetrating arterioles and ascending venules. All postnatal time points are included. Pearson's correlation: Arterioles: $R^2 = 0.4765$, $P = 0.0001$; $n = 25$ penetrating arterioles from five mice. Venules: $R^2 = 0.3535$, $P = 0.0017$; $n = 25$ ascending venules from five mice. (*C*) A schematic summarizing the main findings of this study. Ascending venules are highlighted as the source of angiogenic sprouting. Spatiotemporally distinct forms of sprouting activity are organized to establish the cortical capillary bed between P8 and P12. These structural changes contribute to reduction of blood flow resistance and increased cortical blood flow.

angiogenesis arising from the ascending venules to first form long-range arcs that created the backbone for arteriole-to-venous perfusion. This was followed by short-range endothelial sprouting to form the numerous anastomotic connections between these arcs. By P12, the capillary bed bore resemblance to the capillary architecture seen in the adult brain, indicating that the essential architecture of the capillary bed was established over a remarkably short window of time in the second week of mouse postnatal development.

Prior to these studies, it was unclear how extensive alterations in vascular architecture could be achieved without disruption of blood flow constancy or overt disruption of BBB integrity. Since veins carry lower intravascular pressure and slower flow velocity, the vascular wall is less likely to be breached during the creation of fragile sprouts. Most intriguing is that long-range sprouts destined to connect with high-pressure arterioles appear "pre-formed" with pericyte contact and lumenized endothelial tubes before the introduction of blood flow. These sprouts are ready to become patent upon connection to the arteriole and increase in intravascular pressure. At no point in this process are there vascular "dead ends" or incomplete bridges that would lead to stagnation of flow from an arteriole source. Furthermore, since pericytes interact closely with endothelial cells throughout the angiogenic process (42), it may explain why BBB integrity is largely maintained, perhaps through pericyte–endothelial signaling that suppresses transcytotic leakage (30, 31, 43, 44). Thus, in developing brain capillary networks, there is not an extended window of endothelial immaturity prior to recruitment and coverage by pericytes.

A linchpin in the construction of a perfused capillary network is proper guidance and connection of long-range sprouts to penetrating arterioles. If unsuccessful, all downstream vessels and further anastomotic connections to that sprout would be unperfused. Prior studies from zebrafish have shown that the CXCR4–CXCL12 axis may provide this critical chemotactic signal. Venous-derived angiogenic sprouts in mutants that lack either CXCR4 or its ligand CXCL12 fail to establish links with the basilar artery in microvasculature of the hindbrain (15, 45). Interestingly, *cxcr4a* expression is down-regulated by blood flow, providing a negative-feedback mechanism to reduce growth signals once connection and perfusion is established (15). This mechanism seems to be active in mammals, since CXCR4–CXCL12 disruption leads to misplaced or absent coronary arteries in mouse heart (46). An alternate mechanism for arteriole targeting of sprouts may be repulsion signals derived from ascending venules. Since the venules outnumber and surround penetrating arterioles, this may create a topology of inhibitory cues that direct sprouts toward arterioles. With respect to how long-range vs. short-range growth might be differentially regulated, Ubezio et al. (47) showed that phase transitions in the VEGF-Delta-like four(Dll4)/Notch feedback loop is essential to endothelial cell heterogeneity during shaping of vascular networks. Low levels of VEGF are needed for the expansion and branching of endothelial sprouts, while high levels of VEGF (and Dll4) caused a reduction of the branching, shorter sprouts, and faster lumen formation. This would be in line with long-range sprouts targeting arterioles, where presumably lower VEGF levels around arterioles promote directional growth of the sprout.

While brain capillary networks can be established with surprising speed, this also increases vulnerability to dysregulation and improper development of capillary architecture. There is evidence that abnormal levels of neural activity, both diminished and excessive, can alter angiogenesis and produce lasting alterations in capillary density (13, 48). Impaired vascular architecture can, in turn, fail to provide adequate metabolic supply to neuronal circuits at a critical stage in their development and maturation (49). Furthermore, common complications in the neonate or newborn infant, such as hypoxia–ischemia or apnea of prematurity, can also affect the angiogenic process. Thus, more studies will be needed to study how development of brain capillary beds unfolds in various environmental conditions and disease states.

Materials and Methods

Animals. The Institutional Animal Care and Use Committee at the Seattle Children's Research Institute approved the procedures used in this study. The institutions have accreditation from the Association for Assessment and Accreditation of Laboratory Animal Care, and all experiments were performed within its guidelines.

Tie2-GFP mice were obtained from The Jackson Laboratory (Tg(TIE2GFP) 287Sato/J; Jax ID: 003658). Egfl7-eGFP mice were generated as previously described (27). To create mice with labeled endothelial cells and mural cells, we bred homozygous Tie2-GFP females with PDGFRβ-tdTomato males, the latter of which were generated by crossing heterozygous PDGFRβ-Cre males with Ai14 females (Jax ID: 007914) (33). To increase GFP labeling of endothelial cells, PDGFRβ-tdTomato;Tie2-GFP mice were secondarily bred with homozygous Tie2-GFP mice to achieve homozygosity in the GFP allele. We identified successfully crossed mice by examining for green or red fluorescence using a fluorescent stereoscope (Olympus; SZX10) or a dual fluorescent protein flashlight (NightSea). The day of birth was considered P0. For all studies, we used a roughly equal mixture of male and female offspring. The mice were housed on a 12-h light (7 AM to 7 PM)–dark cycle, with ad libitum access to chow and water.

Surgery. During surgery, body temperature was maintained at 37 °C with a feedback-regulated heat pad (FHC Inc.). Briefly, pups were anesthetized with isoflurane (4–5% induction, 2.5% maintenance) in medical oxygen, and placed in prone position on a heating pad to maintain body temperature (*SI Appendix*, Fig. S1**)**. After cleaning the scalp with betadine and artificial cerebral spinal fluid, a midline incision was made starting between the eyes to just caudal of the ears. A round region of the scalp was removed and sharp forceps were used to gently scrape away the periosteum from the skull surface. Since the skull is not fully formed at the age of window implantation, care was taken to apply minimal force. We first earmarked the location of cranial window placement over the somatosensory cortex, 1–4 mm lateral and 0.5–2.5 mm posterior to bregma (50). A custom-made light-weight aluminum head mount (~0.04 g) was attached to the skull with cyanoacrylate glue (Loctite Instant Adhesive 401) opposite to the hemisphere of window placement for stability during cranial window implantation and subsequent imaging. Solidworks files for mouse pup head mount and holder (compared in size to components for adult mice) are available at https://theshihlab.com/publications/. Once the head bolt was firmly affixed, the exposed skin surrounding the skull was covered with transparent dental cement (Metabond). Then dental cement was applied to the entire assembly, except at the location of window placement, to reinforce the stability of the head mount. As the cement was drying, buprenorphine (Patterson Veterinary) was provided at a dose of 0.05 mg/kg, i.p., for analgesia.

The skull was carefully thinned at the window site by shaving the bone away with the cutting edge of a 31-gauge needle (BD Biosciences; catalog #305109) and a surgical scalpel blade (Fisher Scientific; #15; catalog #22-079-701). Thinning was performed while the skull was dry, but the skull was occasionally moistened with artificial cerebral spinal fluid (ACSF) to examine the window for translucency. The window area was cleaned with ACSF and allowed to dry completely. A drop of cyanoacrylate glue was applied to the window area, carefully avoiding the creation of bubbles, and a precut square piece of glass (2–4 mm) was gently laid down over the thinned region. Dental cement was applied to the edges of the cover glass, and a slight berm was created with the cement to hold water for the dipping lens. To measure the thickness of the skull after successful completion of the window, we imaged the second-harmonic signal of bone using two-photon microscopy in a subset of pups (*SI Appendix*, Fig. S1*I*). This revealed that skull thickness was ~15 μm at the cranial window.

Following cranial window implantation, pups were rubbed with the bedding from the home cage to mask any foreign scent and allowed to completely recover from anesthesia prior to returning to the home cage with the dam, sire, and littermates. During the period when the pup was recovering from anesthesia, small pieces of Metabond dental cement were introduced to the cage to allow the dam and sire to adapt to the smell. Mouse pups receiving window implantation rapidly acclimated to the head mounts. In each litter, we used several mouse pups for imaging, which helped to reduce the likelihood of one pup being singled out and killed by the dam or sire. If bleeding was observed around the windows, or if imaging clarity was lost in the windows, the pups were excluded from the study.

Two-Photon Imaging. Pups were imaged starting the first day after cranial window implantation. Intravenously injected fluorescent dextran dyes of high molecular weight (2 MDa) were used to visualize the cortical microvasculature

and to avoid BBB leakage at early imaging time points. The major dyes used were 2-MDa tetramethylrhodamine (TMR)-dextran [D7139; Thermo Fisher; 2.5% (wt/vol) phosphate buffer saline (PBS)], 2-MDa fluorescein isothiocyanate (FITC)–dextran [FD2000S; Sigma-Aldrich; 1% (wt/vol) PBS], or 2-MDa Alexa 680-dextran [custom conjugated; 5% (wt/vol) PBS] (51). One drawback of using i.v. dyes at the developmental stage studied was dye retention by cells with mast cell-like appearance at the pial surface (*SI Appendix*, Fig. S4) (52). To minimize accumulation of this unwanted signal, we alternated between different dye colors across imaging days. For example, 2-MDa TMR-dextran used at P8, P10, and P12, while 2-MDa Alexa 680-dextran was used at P9 and P11. Pups were anesthetized with isoflurane and secured to a head-fixation apparatus (*SI Appendix*, Fig. S1). Dye injections were made through the retro-orbital vein under deep isoflurane anesthesia (4–5% MAC in medical air). All dyes were injected at a volume of 10–20 μL. Isoflurane was then reduced to ∼1.5% MAC in medical air during imaging, which leaves the pup anesthetized but reactive to light toe pinch.

Two-photon imaging was performed with a Bruker Investigator coupled to a Spectra-Physics Insight ×3 laser. The laser source was tuned to 800-nm excitation to image FITC-dextran. TMR-dextran and Alexa 680-dextran was imaged at 920- or 975-nm excitation, depending upon whether the second channel contained GFP/eGFP (920 nm) or tdTomato (975 nm). Emission bandpass filters were 525/70 nm (green), 595/50 nm (red), and 660/40 nm (far red). High-resolution imaging was performed using a water immersion 20-X, 1.0 N.A. objective lens (Olympus; XLUMPLFLN 20XW). Lateral sampling resolution was 0.4 μm per pixel and axial sampling was 1-μm steps between frames. Line-scans were collected at a rate of ∼1 kHz to collect blood cell velocity data. Typical laser powers used were ∼30 mW at 800 nm for imaging FITC-dextran for blood flow studies, ∼75 mW at 920 nm for GFP (Tie2-GFP mice) and ∼50 mW at 920 nm for eGFP (EGFL7-eGFP mice), and ∼70 mW at 975 nm for combined GFP and tdTomato (PDGFRβ-tdTomato;Tie2-GFP mice) or ∼40 mW at 975 nm for tdTomato alone. Laser power was kept as consistent as possible across imaging time points for each animal. Laser powers were determined at the output of the 20× objective using a laser power meter (Thor Labs; PM100D), with galvanometric mirrors engaged in a full field, 512 × 512 pixel scan covering 16,600 μm^2.

Analysis of In Vivo Imaging Data. High-resolution three-dimensional (3D) images of the cortical vasculature were obtained using Imaris 7.7 software (Bitplane) from raw images. Structural metrics of the microvasculature were quantified with ImageJ (53). Capillary branch/junctional points were counted manually in image stacks and normalized to total image volume. For quantification of BBB leakage, fluorescence intensity of extravasated i.v. dye was measured in image stacks using ImageJ by drawing regions of interest (ROIs) in the parenchyma adjacent to the capillary bed (54). The fluorescence values were evaluated 5–10 min (10 kDa) and 15–30 min (70 kDa) after the injection of the dye. Extravasation of the different-sized dyes were measured at the same locations within the stack. The 2-MDa FITC-dextran was injected first to define the vascular architecture and parenchymal ROIs, followed by Alexa 647-dextran 10 kDa (D22914; Thermo Fisher) and then by Texas Red-dextran 70 kDa (D1864; Thermo-Fisher). The length of angiogenic sprouts and pial venules was measured in 3D using the Simple Neurite Tracer plug-in in ImageJ (https:// imagej.net/Simple_Neurite_Tracer). GFP intensity was quantified with the Measure function in ImageJ and reported in arbitrary units. For vascular branch order classifications, first-order branches were the first microvessel branch emerging from the ascending venule (branch order 0), and each subsequent bifurcation increased branch order by 1. The diameter of angiogenic sprouts was measured manually using the line tool in ImageJ from the i.v. dye image, with multiple measurements taken per sprout and then averaged.

Pericyte somata were manually counted in image stacks collected from PDGFRβ-tdTomato; Tie2-GFP animals. A cell was deemed a pericyte using the following criteria: 1) The cell was PDGFRβ-positive and directly adjacent to i.v. dye-labeled capillary lumen, or Tie2-GFP-positive capillary wall; 2) the cell possessed a small and well-defined ovoid cell body; and 3) there was at least one process extending from the cell body that was comparable in brightness.

For analysis of blood cell velocity from line-scan data, we used custom Matlab software from Kim et al. (55). Lumen diameter for penetrating arterioles and ascending venules was calculated using and ImageJ-based macro called VasoMetrics (56). Blood cell velocity and vessel diameter were then combined using a formula based on Poiseuille's law of laminar flow to obtain the volume flux of blood flow, which is a more complete metric of flow through a single vessel (39).

Image Processing. Only raw images were utilized in data analysis, viewed with ImageJ or MATLAB software. For presentation purposes, images were contrasted and cropped in Adobe Photoshop, one color channel at a time, in a similar manner across all conditions.

Histology. Pups were killed with an intraperitoneal injection of Euthasol (Patterson Veterinary) and immediately perfused transcardially with 4% paraformaldehyde in 0.1 M PBS. Brains were extracted, postfixed overnight, and subsequently immersed in 30% sucrose in 0.1 M PBS for up to 48 h. Coronal sections (300 μm) cut on a cryostat (Leica; CM3050S) were collected in PBS with 0.01% sodium azide and stored at 4 °C until use. Slices were first incubated for 2 h in blocking solution consisting of PBS with 5% (vol/vol) goat serum (S-1000; Vector Labs) and 0.3% (vol/vol) Triton X-100 (Sigma). Then the slices were transferred to well plates with primary antibody or lectin diluted into PBS with 5% (vol/vol) goat serum and 0.2% (vol/vol) Triton X-100 to incubate at 4 °C with nutation. To label microglia, slices were incubated with ionized calcium-binding protein 1 (Iba-1, 1:250 dilution, 019-19741; Wako; microglia marker) primary antibody for 4 d. To label microvasculature, slices were incubated with Isolectin GS-IB4-Alexa Fluor 647 Conjugate (Ib4, 1:250 dilution; I32450; Fisher Scientific; endothelial marker) for 5 d. In both cases, the slices were then washed five times ×5 min with 0.1 M PBS. With Iba-1 immunostaining, slices were then transferred to secondary antibody Alexa Fluor 647 (1:500 dilution; A32733; Thermo Fisher Scientific) for 2 h at room temperature. After washing, slices were mounted, dried, and coverslip-sealed with DAPI Fluoromount-G (catalog #0100-20; Southern Biotechnology). High-resolution confocal images were collected using an Olympus FV10i confocal microscope using either a 20×, 1.2 N.A. water objective, or a 40×, 1.2 N.A. oil immersion objective. Images were collected with dimensions of 1,024 × 1,024 pixels with averaging of every four frames.

Analysis of Histological Data. The histological quantifications were performed by an investigator blinded to the animal condition. To address the possibility of neuroinflammation caused by the surgery and imaging, Iba-1–stained image stacks of each brain hemispheres were selected using ImageJ (776 × 776 × 25-μm volume examined per hemisphere). The number of Iba-1–positive cells at the cortical field of view were counted using cell counter plugin of ImageJ. To compare capillary density between surgery and nonsurgery animals, image stack projections were selected from each Ib4-stained epifluorescence image collected (two to four ROIs per animal; 776 × 776 × 100-μm volume for each region) using ImageJ. The images were then loaded into AngioTool software (57), the scale was calibrated in accordance with our microscope collection parameters, and the settings "remove small particles" and "fill holes" were selected. AngioTool provided data on the length of vessels in the ROI.

Statistics. Statistical analyses were performed using GraphPad Prism 8 software. Statistical tests and details are provided in the figure legends. Tests of normality were first performed to validate the use of parametric tests.

Data Availability. All study data are included in the article and/or supporting information.

ACKNOWLEDGMENTS. We appreciate the helpful comments and discussion of Stefan Stamenkovic, Sandra Juul, and Mark W. Majesky. We are grateful to Madeline Kilby and Taryn Tieu for the vivarium support and colony management. We also thank Tiago Figueiredo for creating the artwork used in Figs. 1*A* and 7*C* (https://www.behance.net/TiagoFigueiredoGD). Our work is supported by grants to A.Y.S. from the NIH/National Institute of Neurological Disorders and Stroke (NS096997, NS106138, and NS097775) and NIH/National Institute on Aging (AG063031 and AG062738) and to H.S. from the NIH/National Institute of Mental Health (MH083680). V.C.-S. is supported by awards from the American Heart Association (20POST35160001) and Luso-American Development Foundation (2017/165).

1. P. Carmeliet, R. K. Jain, Molecular mechanisms and clinical applications of angiogenesis. *Nature* **473**, 298–307 (2011).
2. I. G. Gould, P. Tsai, D. Kleinfeld, A. Linninger, The capillary bed offers the largest hemodynamic resistance to the cortical blood supply. *J. Cereb. Blood Flow Metab.* **37**, 52–68 (2017).
3. F. Schmid, P. S. Tsai, D. Kleinfeld, P. Jenny, B. Weber, Depth-dependent flow and pressure characteristics in cortical microvascular networks. *PLOS Comput. Biol.* **13**, e1005392 (2017).
4. D. A. Hartmann *et al*., Brain capillary pericytes exert a substantial but slow influence on blood flow. *Nat. Neurosci.* **24**, 633–645 (2021).

5. S. N. Jespersen, L. Østergaard, The roles of cerebral blood flow, capillary transit time heterogeneity, and oxygen tension in brain oxygenation and metabolism. *J. Cereb. Blood Flow Metab.* **32**, 264–277 (2012).
6. B. T. Hawkins, T. P. Davis, The blood-brain barrier/neurovascular unit in health and disease. *Pharmacol. Rev.* **57**, 173–185 (2005).
7. T. A. Longden *et al*., Capillary K^+-sensing initiates retrograde hyperpolarization to increase local cerebral blood flow. *Nat. Neurosci.* **20**, 717–726 (2017).
8. A. M. Nikolakopoulou *et al*., Pericyte loss leads to circulatory failure and pleiotrophin depletion causing neuron loss. *Nat. Neurosci.* **22**, 1089–1098 (2019).
9. I. Krolo, A. G. Hudetz, Remodeling of the leptomeningeal microvascular plexus in neonatal rats. *Adv. Exp. Med. Biol.* **454**, 349–354 (1998).
10. J. A. Anstrom *et al*., Anatomical analysis of the developing cerebral vasculature in premature neonates: Absence of precapillary arteriole-to-venous shunts. *Pediatr. Res.* **52**, 554–560 (2002).
11. D. B. Wang, N. C. Blocher, M. E. Spence, C. M. Rovainen, T. A. Woolsey, Development and remodeling of cerebral blood vessels and their flow in postnatal mice observed with in vivo videomicroscopy. *J. Cereb. Blood Flow Metab.* **12**, 935–946 (1992).
12. R. Harb, C. Whiteus, C. Freitas, J. Grutzendler, In vivo imaging of cerebral microvascular plasticity from birth to death. *J. Cereb. Blood Flow Metab.* **33**, 146–156 (2013).
13. B. Lacoste *et al*., Sensory-related neural activity regulates the structure of vascular networks in the cerebral cortex. *Neuron* **83**, 1117–1130 (2014).
14. K. Red-Horse, H. Ueno, I. L. Weissman, M. A. Krasnow, Coronary arteries form by developmental reprogramming of venous cells. *Nature* **464**, 549–553 (2010).
15. J. Bussmann, S. A. Wolfe, A. F. Siekmann, Arterial-venous network formation during brain vascularization involves hemodynamic regulation of chemokine signaling. *Development* **138**, 1717–1726 (2011).
16. C. Xu *et al*., Arteries are formed by vein-derived endothelial tip cells. *Nat. Commun.* **5**, 5758 (2014).
17. M. Fruttiger, Development of the mouse retinal vasculature: Angiogenesis versus vasculogenesis. *Invest. Ophthalmol. Vis. Sci.* **43**, 522–527 (2002).
18. K. Red-Horse, A. F. Siekmann, Veins and arteries build hierarchical branching patterns differently: Bottom-up versus top-down. *BioEssays* **41**, e1800198 (2019).
19. A. Letourneur, V. Chen, G. Waterman, P. J. Drew, A method for longitudinal, transcranial imaging of blood flow and remodeling of the cerebral vasculature in postnatal mice. *Physiol. Rep.* **2**, e12238 (2014).
20. B. D. Semple, K. Blomgren, K. Gimlin, D. M. Ferriero, L. J. Noble-Haeusslein, Brain development in rodents and humans: Identifying benchmarks of maturation and vulnerability to injury across species. *Prog. Neurobiol.* **106-107**, 1–16 (2013).
21. T. N. Sato *et al*., Distinct roles of the receptor tyrosine kinases Tie-1 and Tie-2 in blood vessel formation. *Nature* **376**, 70–74 (1995).
22. T. Motoike *et al*., Universal GFP reporter for the study of vascular development. *Genesis* **28**, 75–81 (2000).
23. A. L. Wong *et al*., Tie2 expression and phosphorylation in angiogenic and quiescent adult tissues. *Circ. Res.* **81**, 567–574 (1997).
24. M. R. Kelly-Goss *et al*., Dynamic, heterogeneous endothelial Tie2 expression and capillary blood flow during microvascular remodeling. *Sci. Rep.* **7**, 9049 (2017).
25. J. Nguyen, N. Nishimura, R. N. Fetcho, C. Iadecola, C. B. Schaffer, Occlusion of cortical ascending venules causes blood flow decreases, reversals in flow direction, and vessel dilation in upstream capillaries. *J. Cereb. Blood Flow Metab.* **31**, 2243–2254 (2011).
26. Z. J. Taylor *et al*., Microvascular basis for growth of small infarcts following occlusion of single penetrating arterioles in mouse cortex. *J. Cereb. Blood Flow Metab.* **36**, 1357–1373 (2016).
27. K. Bambino, L. A. Lacko, K. A. Hajjar, H. Stuhlmann, Epidermal growth factor-like domain 7 is a marker of the endothelial lineage and active angiogenesis. *Genesis* **52**, 657–670 (2014).
28. L. Poissonnier, G. Villain, F. Soncin, V. Mattot, Egfl7 is differentially expressed in arteries and veins during retinal vascular development. *PLoS One* **9**, e90455 (2014).
29. M. Hellström, M. Kalén, P. Lindahl, A. Abramsson, C. Betsholtz, Role of PDGF-B and PDGFR-beta in recruitment of vascular smooth muscle cells and pericytes during embryonic blood vessel formation in the mouse. *Development* **126**, 3047–3055 (1999).
30. R. Daneman, L. Zhou, A. A. Kebede, B. A. Barres, Pericytes are required for blood-brain barrier integrity during embryogenesis. *Nature* **468**, 562–566 (2010).
31. A. Armulik *et al*., Pericytes regulate the blood-brain barrier. *Nature* **468**, 557–561 (2010).
32. L. E. Benjamin, I. Hemo, E. Keshet, A plasticity window for blood vessel remodelling is defined by pericyte coverage of the preformed endothelial network and is regulated by PDGF-B and VEGF. *Development* **125**, 1591–1598 (1998).
33. D. A. Hartmann *et al*., Pericyte structure and distribution in the cerebral cortex revealed by high-resolution imaging of transgenic mice. *Neurophotonics* **2**, 041402 (2015).
34. R. I. Grant *et al*., Organizational hierarchy and structural diversity of microvascular pericytes in adult mouse cortex. *J. Cereb. Blood Flow Metab.* **39**, 411–425 (2019).
35. V. Coelho-Santos, A. Y. Shih, Postnatal development of cerebrovascular structure and the neurogliovascular unit. *Wiley Interdiscip. Rev. Dev. Biol.* **9**, e363 (2020).
36. P. Blinder *et al*., The cortical angiome: An interconnected vascular network with noncolumnar patterns of blood flow. *Nat. Neurosci.* **16**, 889–897 (2013).
37. A. Y. Shih *et al*., The smallest stroke: Occlusion of one penetrating vessel leads to infarction and a cognitive deficit. *Nat. Neurosci.* **16**, 55–63 (2013).
38. A. Y. Shih *et al*., Two-photon microscopy as a tool to study blood flow and neurovascular coupling in the rodent brain. *J. Cereb. Blood Flow Metab.* **32**, 1277–1309 (2012).
39. A. Y. Shih *et al*., Active dilation of penetrating arterioles restores red blood cell flux to penumbral neocortex after focal stroke. *J. Cereb. Blood Flow Metab.* **29**, 738–751 (2009).
40. C. M. Rovainen, D. B. Wang, T. A. Woolsey, Strobe epi-illumination of fluorescent beads indicates similar velocities and wall shear rates in brain arterioles of newborn and adult mice. *Microvasc. Res.* **43**, 235–239 (1992).
41. R. Wild *et al*., Neuronal sFlt1 and Vegfaa determine venous sprouting and spinal cord vascularization. *Nat. Commun.* **8**, 13991 (2017).
42. L. B. Payne *et al*., The pericyte microenvironment during vascular development. *Microcirculation* **26**, e12554 (2019).
43. A. Ben-Zvi *et al*., Mfsd2a is critical for the formation and function of the blood-brain barrier. *Nature* **509**, 507–511 (2014).
44. J. Chen *et al*., CD146 coordinates brain endothelial cell-pericyte communication for blood-brain barrier development. *Proc. Natl. Acad. Sci. U.S.A.* **114**, E7622–E7631 (2017).
45. M. Fujita *et al*., Assembly and patterning of the vascular network of the vertebrate hindbrain. *Development* **138**, 1705–1715 (2011).
46. S. Ivins *et al*., The CXCL12/CXCR4 axis plays a critical role in coronary artery development. *Dev. Cell* **33**, 455–468 (2015).
47. B. Ubezio *et al*., Synchronization of endothelial Dll4-Notch dynamics switch blood vessels from branching to expansion. *eLife* **5**, e12167 (2016).
48. C. Whiteus, C. Freitas, J. Grutzendler, Perturbed neural activity disrupts cerebral angiogenesis during a postnatal critical period. *Nature* **505**, 407–411 (2014).
49. J. Shen, M. T. Colonnese, Development of activity in the mouse visual cortex. *J. Neurosci.* **36**, 12259–12275 (2016).
50. G. Paxinos, G. M. Halliday, C. Watson, Y. Koutcherov, H. U. Wang, *Atlas of the Developing Mouse Brain at E17.5, P0 and P6* (Elsevier, 2007).
51. B. Li *et al*., Two-photon microscopic imaging of capillary red blood cell flux in mouse brain reveals vulnerability of cerebral white matter to hypoperfusion. *J. Cereb. Blood Flow Metab.* **40**, 501–512 (2020).
52. M. Khalil *et al*., Brain mast cell relationship to neurovasculature during development. *Brain Res.* **1171**, 18–29 (2007).
53. C. A. Schneider, W. S. Rasband, K. W. Eliceiri, NIH Image to ImageJ: 25 years of image analysis. *Nat. Methods* **9**, 671–675 (2012).
54. D. Zhu *et al*., Protein S controls hypoxic/ischemic blood-brain barrier disruption through the TAM receptor Tyro3 and sphingosine 1-phosphate receptor. *Blood* **115**, 4963–4972 (2010).
55. T. N. Kim *et al*., Line-scanning particle image velocimetry: An optical approach for quantifying a wide range of blood flow speeds in live animals. *PLoS One* **7**, e38590 (2012).
56. K. P. McDowell, A. A. Berthiaume, T. Tieu, D. A. Hartmann, A. Y. Shih, VasoMetrics: Unbiased spatiotemporal analysis of microvascular diameter in multi-photon imaging applications. *Quant. Imaging Med. Surg.* **11**, 969–982 (2020).
57. E. Zudaire, L. Gambardella, C. Kurcz, S. Vermeren, A computational tool for quantitative analysis of vascular networks. *PLoS One* **6**, e27385 (2011).